Computers and Geotechnics 195 (2026) 108053

Contents lists available at ScienceDirect

Computers and Geotechnics

journal homepage: www.elsevier.com/locate/compgeo

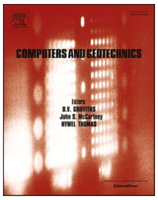

Research Paper

Effect of pile corner rounding on local scour around offshore wind turbine foundations in sands using CFD–DEM

Xiangyi Meng [a], Yifan Lu [a], Xiaoming Feng [a], Guizhong Tian [a], Yadong Zhu [a], Zhongqiu Mu [b,*]

[a] College of Mechanical Engineering, Jiangsu University of Science and Technology, Zhenjiang 212100, China
[b] Nanjing Institute of Agricultural Mechanization, Ministry of Agriculture and Rural Affairs, Nanjing 210000, China

ARTICLE INFO

Keywords:
Local scour
Offshore wind turbine
CFD-DEM
Rounded corner ratio
Scour depth prediction

ABSTRACT

Local scour, caused by flow-induced sediment erosion around piles, poses a significant threat to the stability of offshore wind turbine foundations. Although corner rounding has been proposed as an effective scour mitigation measure, the quantitative influence of rounded corner ratios (R/D) on local scour development remains insufficiently understood, thereby limiting reliable prediction and design of rounded square piles. In this study, local scour around rounded square piles is investigated using a coupled CFD–DEM numerical model, with analyses of scour evolution, bed morphology, sediment particle dynamics, and near-bed flow structures under different R/D conditions. In this study, a coupled CFD–DEM numerical model is employed to investigate local scour around rounded square piles under various R/D conditions. The results show that rounding corners effectively reduces scour by regulating near-bed flow structures and restraining sediment movement. An optimum anti-scour performance is identified at $R/D = 0.3$, which significantly reduces the equilibrium scour depth compared to a sharp-cornered pile. Based on the simulation data, an empirical scour prediction model incorporating R/D as a governing parameter is developed, and its validation shows satisfactory predictive accuracy. This study provides a reliable basis for quantitative scour assessment and design optimization of offshore wind turbine foundations with complex cross-sections.

1. Introduction

Offshore wind turbines have been widely deployed in recent years (Liu et al., 2026). However, foundation local scour remains a critical challenge to their long-term safe operation, as it may induce structural instability or even complete overturning (Wang et al., 2023). Local scour is defined as the erosion of riverbed sediments around submerged structures, such as pile foundations, caused by flow disturbance. This process progressively removes surrounding sediments, significantly reducing the effective embedment depth of the foundation and consequently compromising both the vertical and lateral load-bearing capacity of the structure, thereby threatening its overall stability (Y. Zhang et al., 2025). Specifically, scour can lower the natural frequency of the structure, diminish pile capacity (Prendergast et al., 2015), and exacerbate structural deformation (Li et al., 2024). As a critical sediment transport mechanism, it also poses a threat to the long-term stability of hydraulic structures like bridge piers. The formation of local scour is primarily governed by the evolution and interaction of complex vortex systems, including horseshoe vortices, downflow, and lee-wake vortices, as shown in Fig. 1 (Zhang et al., 2025; Chen, 2026). In practice, scour-induced structural failures are common. For instance, two pile foundations at the Robin Rigg offshore wind farm were decommissioned due to local scour issues after six years of operation (Menéndez-Vicente et al., 2023). In the bridge engineering sector, approximately 58% of collapse incidents are directly related to scour. Although systematic scour risk for offshore wind structures has not yet fully emerged due to their relatively short service history, long-term observational data from bridge engineering indicate that such foundations will face increasingly severe scour challenges in the future. The development of local scour is influenced by multiple factors, including sediment properties, structural geometry, and flow conditions, among which structural geometry is widely recognized as one of the key controlling parameters (Mir et al., 2019). Therefore, investigating the influence of pile structural configuration on scour characteristics is essential for identifying optimized designs and providing guidance for anti-scour measures.

The geometric shape of the pile directly controls the surrounding flow field and governs the development of the scour pit. Optimizing the cross-sectional shape of the pile based on hydrodynamic characteristics

---

* Corresponding author.
E-mail address: muzhongqiu@caas.cn (Z. Mu).

https://doi.org/10.1016/j.compgeo.2026.108053
Received 7 January 2026; Received in revised form 13 February 2026; Accepted 5 March 2026

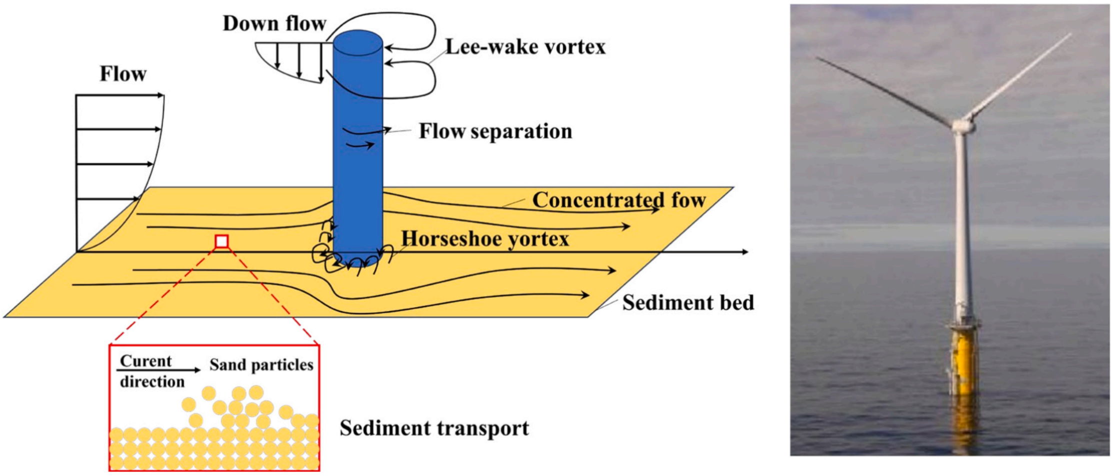

Fig. 1. Diagram of the flow structure around piles.

is crucial for scour prevention and control. Although the scour mechanisms around circular piles have been extensively investigated due to their widespread use in foundation and pipeline engineering (Jalal and Hassan, 2020; Ma et al., 2023; Ma et al., 2024), research on non-circular cross-sections remains relatively limited (Bordbar et al., 2021). It is noteworthy that non-circular sections such as square piles, owing to their superior bending stiffness compared to circular sections, have been widely employed in port engineering, coastal protection, and composite abutments (Amini Baghbadorani et al., 2018; Du et al., 2022). However, the blunt-body characteristics of square piles induce fixed flow separation, leading to strong vortex shedding and enhanced turbulence, which exacerbates local scour and may trigger vortex-induced vibrations, jeopardizing long-term structural safety. To balance structural performance and hydrodynamic behavior, the adoption of rounded square piles is regarded as an effective synergistic optimization strategy (Li et al., 2023). Studies demonstrate that appropriate corner rounding not only improves stress distribution across the section and enhances component load-bearing capacity, but also delays flow separation, suppresses the development of horseshoe vortex, and attenuates wake vorticity, thereby significantly mitigating scour progression (Yang et al., 2024; Li et al., 2025). Overall, local scour around standard cross-sectional piles, such as circular and square, has been widely studied. However research on the underlying mechanisms and scour characteristics of non-standard cross-sections, such as rounded square piles, remains unclear. This limitation hinders accurate prediction of local scour patterns around offshore wind turbine piles. The development of

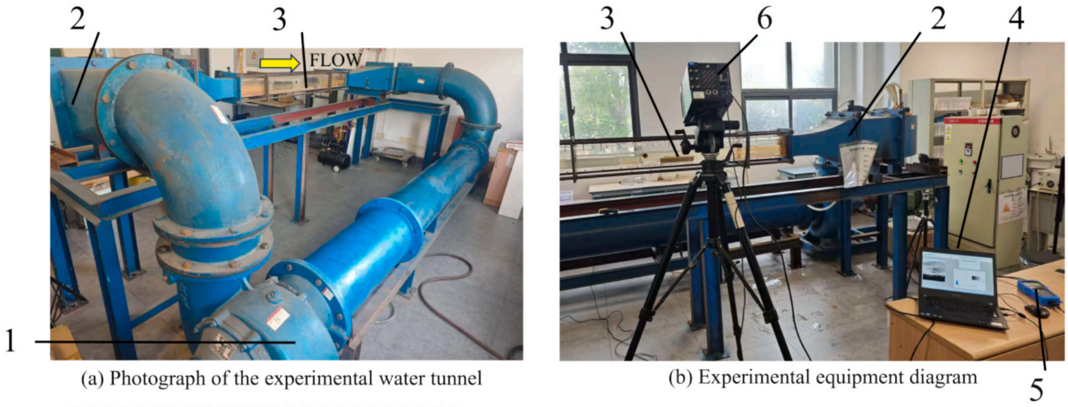

(a) Photograph of the experimental water tunnel

(b) Experimental equipment diagram

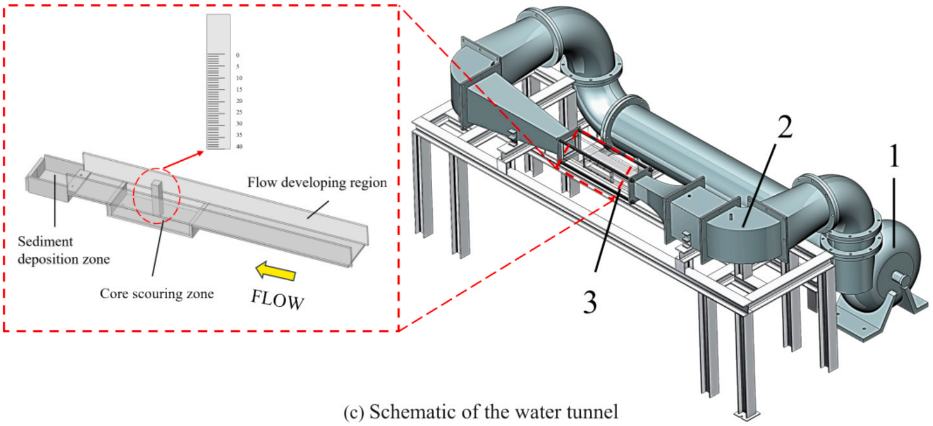

(c) Schematic of the water tunnel

Fig. 2. Experimental water tunnel system. 1: Water pump; 2: Settling section; 3: Test section; 4: Computer; 5: Ultrasonic flowmeter; 6: Camera.

effective scour protection measures is therefore constrained.

In recent years, advancements in computational performance and numerical simulation technology have established numerical modeling as a valuable approach for analyzing and predicting local scour mechanisms (Olsen and Melaaen, 1993; Roulund et al., 2005; Liu and García, 2008). Among these methods, the coupled CFD-DEM (Computational Fluid Dynamics-Discrete Element Method) has garnered significant attention due to its ability to accurately capture the microscopic motion of sediment particles under fluid action (Baykal et al., 2017; Li et al., 2021). For instance, Li successfully simulated the micromechanical dynamics of sediment during local scour around a pile using this approach (Li and Tao, 2018). Similarly, Song investigated the influence of particle shape on scour evolution, demonstrating that the scour pattern around subsea pipelines is significantly affected by interparticle friction conditions (Song and Park, 2022). The introduction of CFD-DEM effectively addresses the limitations of traditional experimental methods in tracking particle trajectories, force states, and other microscopic information, as well as in flow field visualization (Zheng et al., 2024). Previous studies have examined how the cross-sectional shape of a single pile influences flow characteristics and scour evolution. Their findings indicate that rounded square piles can potentially reduce scour risk compared to conventional square piles.

However, the relationship between the rounded-corner ratio and local scour characteristics has not yet been clearly quantified, which limits the identification of an optimal pile geometry for practical engineering applications aimed at mitigating scour development. Therefore, it is necessary to investigate the influence of corner rounding on local scour behavior and to establish a corresponding prediction model for scour depth, so as to provide guidance for structural design and geometry optimization of pile foundations.

In this study, a coupled CFD–DEM numerical model is adopted to simulate the water–sediment–structure interaction during scour development. Based on this framework, particle motion characteristics, kinetic energy evolution, and flow-field structures are analyzed under different rounded corner ratios (R/D), so as to clarify the influence of corner rounding on scour mitigation. On this basis, a geometric modification function with R/D as the governing parameter is incorporated into an empirical formula, from which a modified predictive formula for local scour depth is proposed. The proposed model is further validated under multiple operating conditions, with the results demonstrating satisfactory predictive accuracy. This provides a reliable basis for scour risk assessment and protective design of piles with complex cross-sections.

2. Methodology

2.1. Experiment setup and model parameters

The experimental study was conducted in a high-speed recirculating water flume at the laboratory of Jiangsu University of Science and Technology. The overall layout of the flume is shown in Fig. 2(a). A stepless variable-speed motor drives the mixed-flow pump unit, allowing continuous adjustment of the flow velocity within the range of 0.4–2.0 m/s. Flow conditioning is achieved through a stabilization section equipped with turning vanes and a honeycomb flow straightener in sequence, ensuring that the turbulence intensity in the test section remains below 1%. The test section, constructed entirely of transparent acrylic plates to facilitate flow observation and water depth measurement, has dimensions of 1800 mm (streamwise) × 128 mm (normal) × 128 mm (spanwise). Fig. 2(c) shows the detailed structure of the test section, which primarily consists of three components: a flow development section, a core scouring section, and a sediment deposition section. All tests were performed under clear-water scour conditions in the closed-circuit flume. A flow velocity of 0.4 m/s was adopted, based on typical coastal current velocities in nearshore environments. Flow velocity was measured with a KZ-2000H ultrasonic flowmeter obtained from Kezhou Co., Ltd., China. with a sampling frequency of 20 Hz, a measurement accuracy of ±1%, and a lower measurement limit of 0.2 m/s. The sensor was installed in a sufficiently long straight pipe section upstream of the test area to ensure fully developed flow. Prior to the experiments, the measurement system was calibrated against a standard flowmeter to ensure data reliability (Fig. 2(b)). Scour morphology around the pile was monitored using a transparent scale attached to the pile surface, with a minimum division of 5 mm. To achieve more precise observation of the scouring process while minimizing manual reading errors, a high-speed camera (frame rate: 100 fps) was employed to record the entire scour process. The temporal evolution of the scour pit morphology was obtained through post-processing of the captured images. All experiments were conducted at a controlled room temperature of 20 ± 2 °C. Pure water was used as the flow medium, and the sediment bed was composed of uniform quartz sand with a median grain size $d_{50} = 1$ mm. The model pile had a diameter of 15 mm, and the surrounding soil was configured with a core scour zone measuring 30 mm in depth, 90 mm in width, and 165 mm in length. Each test was repeated three times to verify the reproducibility of the results.

2.2. Numerical simulations

2.2.1. Discrete element method (DEM) model

In this paper, the commercial EDEM (Altair Engineering Inc., Troy, MI, USA) software is used to simulate and analyse the local scour process of offshore wind pile foundations (Meng et al., 2025). Under the Discrete Element Method framework, the sediment surrounding the pile is represented as an assembly of numerous independent discrete particles. The motion response of each particle under external loading is governed by Newtonian mechanics, with its translational and rotational behaviors controlled by Newton's second law and Euler's second law, respectively, as expressed in Eq. (1) and (2). To simplify the numerical calculations and maintain model feasibility, the actual sediment particles are idealized as spherical entities in this study. This modeling approach enables the systematic tracking of key kinematic parameters, including displacement, velocity and acceleration for each individual particle (Hu et al., 2019).

$$m_i \frac{\mathrm{d}U_i^p}{\mathrm{d}t} = \sum_{j=1}^{n_i^c} \left(\mathrm{F}_{ij}^c + \mathrm{F}_i^g + \mathrm{F}_{pi}^f\right) \tag{1}$$

$$I_i \frac{\mathrm{d}\omega_i}{\mathrm{d}t} = \sum_c \tag{2}$$

In this model, $\mathrm{m_i}$ and $\mathrm{I_i}$ represent the mass and moment of inertia of particle i, respectively; $\mathrm{U_i}$ and ω_i denote its translational velocity and angular velocity vectors, respectively. The contact force $\mathrm{F_{ij}^c}$ between particle i and its neighboring particle j consists of an elastic component and a damping component. The total number of particles in contact with particle i is denoted as $\mathrm{n_i^c}$. $\mathrm{M_{ij}^t}$ and $\mathrm{M_{ij}^r}$ represent the moments generated by the tangential friction force and the rolling friction force exerted by particle j on particle i, respectively. Additionally, $\mathrm{F_i^g}$ denotes the gravitational force acting on the particle. Where $\mathrm{F_{pi}^f}$ is the total fluid force acting on the particle i. To simulate the interlocking effect induced by natural sediment particles, a constant-direction torque model is employed, which is calculated according to the following equation (Zhou et al., 1999):

$$\mathrm{M}_{ij}^r = -\frac{\omega_{ij}}{\|\omega_{ij}\|} \mu_r \left|\mathrm{F}_{ij}^n\right| \mathrm{R}_{ij} \tag{3}$$

In the governing Eq. (3), ω_{ij} denotes the relative angular velocity between particles i and j. The Frobenius norm of ω_{ij}, denoted as $\|\omega_{ij}\|$, is defined by $\|\omega_{ij}\| = \sqrt{(\omega_{ij} : \omega_{ij})}$. The coefficient of rolling resistance is represented by μ_r, and the magnitude of the normal contact force $\mathrm{F_{ij}^n}$ is given by $|F_{ij}^{n}|$. The rolling radius R_{ij} is expressed as $R_{ij} = r_i r_j/(r_i + r_j)$, where r_i and r_j are the radii of the contacting particles i and j, respectively. The torque M_{ij}^{t} resulting from the tangential frictional force exerted by particle j on particle i can be formulated as:

$$M_{ij}^{t} = R_{ij} \times F_{ij}^{t} \tag{4}$$

In this formulation, R_{ij} represents the displacement vector pointing from the center of particle i to the contact point with particle j, and F_{ij}^{t} corresponds to the tangential frictional force acting between particles i and j. The magnitude of the tangential force F_{ij}^{t} is constrained by the inequality $\|F_{ij}^{t}\| \leq \mu_t \|F_{ij}^{n}\|$, where μ_t denotes the coefficient of tangential friction.

Interparticle contact behavior is described using a Hertz-Mindlin-based non-slip soft-sphere model (Mindlin and Deresiewicz, 1953). In this model, the total contact force can be decomposed into normal and tangential components, expressed as follows:

$$F_{ij}^{c} = F_{ij}^{n} + F_{ij}^{t} \tag{5}$$

The normal force F_{ij}^{n} consists of a spring force and a damping force, calculated as follows:

$$F_{ij}^{n} = \left(k_n \delta_{ij}^{n} - \gamma_n v_{ij}^{n}\right) \tag{6}$$

where δ_{ij}^{n} is the normal overlapping distance, v_{ij}^{n} is the normal component of the relative velocity, k_n and γ_n are the elastic constant and viscoelastic damping constant for normal contact, respectively.

The tangential force F_{ij}^{t} incorporates both a shear component and a damping component, and its magnitude is limited by the Coulomb friction criterion.

$$F_{ij}^{t} = \begin{cases} k_t \delta_{ij}^{t} - \gamma_t v_{ij}^{t} \left(F_{ij}^{t} \leq \mu F_{ij}^{n}\right) \\ \mu F_{ij}^{n} \left(F_{ij}^{t} = \mu F_{ij}^{n}\right) \end{cases} \tag{7}$$

where δ_{ij}^{t} is the tangential displacement vector, v_{ij}^{t} is the tangential component of the relative velocity, μ is the friction coefficient, k_t and γ_t are the elastic constant and viscoelastic damping constant for tangential contact, respectively.

2.2.2. *Computational fluid dynamics (CFD) model*

In the present work, the fluid phase was modeled using a commercial computational fluid dynamics package (Ansys, Inc., Canonsburg, PA, USA). As the physical scenario under consideration involves only mass and momentum conservation, the incompressible form of the Navier–Stokes Equation was applied. Within the coupled CFD–DEM solution framework, the set of governing equation for the fluid phase incorporates the influence exerted by the particulate phase (Ma et al., 2023). Accordingly, the continuity and momentum equation for an incompressible viscous fluid are adapted in the following form:

$$\frac{\partial(\varepsilon_k \rho_k)}{\partial t} + \nabla \cdot (\varepsilon_k \rho_k \boldsymbol{u}_k) = 0 \tag{8}$$

$$\frac{\partial(\varepsilon_k \rho_k \boldsymbol{u}_k)}{\partial t} + \nabla \cdot (\varepsilon_k \rho_k \mu_k \boldsymbol{u}_k) = -\nabla p + \nabla \cdot (\mu_k \varepsilon_k \nabla \boldsymbol{u}_k) - \varepsilon_k \rho_k g - S \tag{9}$$

In the governing Eq. (8) and (9), t denotes time, ρ_k is the fluid density, ε_k represents the porosity, S refers to the momentum source term, u_k indicates the fluid velocity vector, μ_k is the dynamic viscosity, and p signifies the pressure. Within the CFD-DEM framework, the interaction between the fluid and particle phases is modeled by incorporating the momentum source term S, which accounts for the drag force ($Fp_{,i}$) arising from the relative velocity between the phases. The expression for the momentum source term is given as follows:

$$S = \frac{1}{\nabla x \nabla y \nabla z} \sum_{i=1}^{n_i} Fp, i \tag{10}$$

In this formulation, ∇x, ∇y and ∇z denote the control lengths in the respective coordinate directions. The drag force Fp,i is evaluated using the following expression (Li et al., 2012):

$$F_{p,i} = 0.5 C_D \rho_k A(\boldsymbol{u}_k - v_i)|\boldsymbol{u}_k - v_i| \varepsilon_k^{-(\boldsymbol{x}+1)} \tag{11}$$

where $\chi = 3.7 - 0.65\exp\left[\frac{-(1.5 - log_{10}Re)^2}{2}\right]$, $C_D = \left(0.63 + 4.8/Re^{0.5}\right)^2$, Re is Reynolds number, and C_D is fluid resistance coefficient (Li et al., 2012).

The renormalization group (RNG) *k-ε* model was selected to simulate the weak turbulence and high-shear flow fields around the pile scour:

$$\frac{\partial k}{\partial t} + \frac{1}{V_f} \overline{u}_j A_j \frac{\partial k}{\partial x_i} = P_k + B + Diff_k - \varepsilon \tag{12}$$

$$\frac{\partial \varepsilon}{\partial t} + \frac{1}{V_f} \overline{u}_j A_j \frac{\partial k}{\partial x_i} = \frac{C_1 \varepsilon}{k}(P_k + C_3 B) + Diff_\epsilon - \frac{C_2 \varepsilon^2}{k} \tag{13}$$

In the *k-ε* turbulence model, *k* denotes the turbulent kinetic energy, while *ε* represents the rate of turbulent energy dissipation. The terms P_k and *B* correspond to the shear production and buoyancy-driven production of turbulent kinetic energy, respectively. Furthermore, $Diff_k$ and $Diff_\epsilon$ signify the effective diffusivity for *k* and *ε*, respectively (Zhu et al., 2025).

2.3. *Coupling procedure*

The CFD-DEM coupling model serves as an important numerical tool for investigating the dynamic behavior of fluid–particle multiphase systems (Yazdanfar et al., 2021). By integrating the modeling capability of computational fluid dynamics for continuous media with the analytical advantage of the discrete element method for particle motion. This approach provides a comprehensive description of the interactions between the fluid and particle phases, as well as the dynamic evolution of the system. (Zhang et al., 2026). This coupled approach is implemented based on an alternating numerical solution process. The aim of this procedure is to achieve more precise observation of the scouring process while minimizing manual reading errors. In this study, a coupled solid–liquid two-phase flow model was constructed based on the Eulerian-Lagrangian framework. The fluid phase is treated as a continuous medium and solved using the Eulerian approach in ANSYS Fluent, with its flow governed by the mass and momentum conservation equations. The realizable k-ε turbulence model is employed to simulate the flow characteristics. The discrete sand particle phase is tracked via the Lagrangian method in EDEM according to Newton's second law. The bidirectional coupling data exchange between the two phases (including fluid flow information, particle motion, and their momentum and energy attributes) is achieved through User-Defined Functions (UDFs) developed on the Visual Studio platform within the Fluent–EDEM coupling interface. The specific procedure of the data exchange is as follows: First, the DEM module calculates the contact forces and fluid-induced forces acting on the particles, solves the governing equations of particle motion, and subsequently updates the particle velocities and displacements. Subsequently, based on the particle positions, the momentum exchange source terms are assembled, and the local solid-phase volume fraction is computed, which are then passed to the CFD module. The CFD module solves the fluid momentum equations using the received source terms and volume fraction information, obtains the updated spatial distributions of the velocity field and pressure field, and iterates until the flow field converges. Finally, the calculated fluid–particle interaction forces are fed back to the DEM module to update

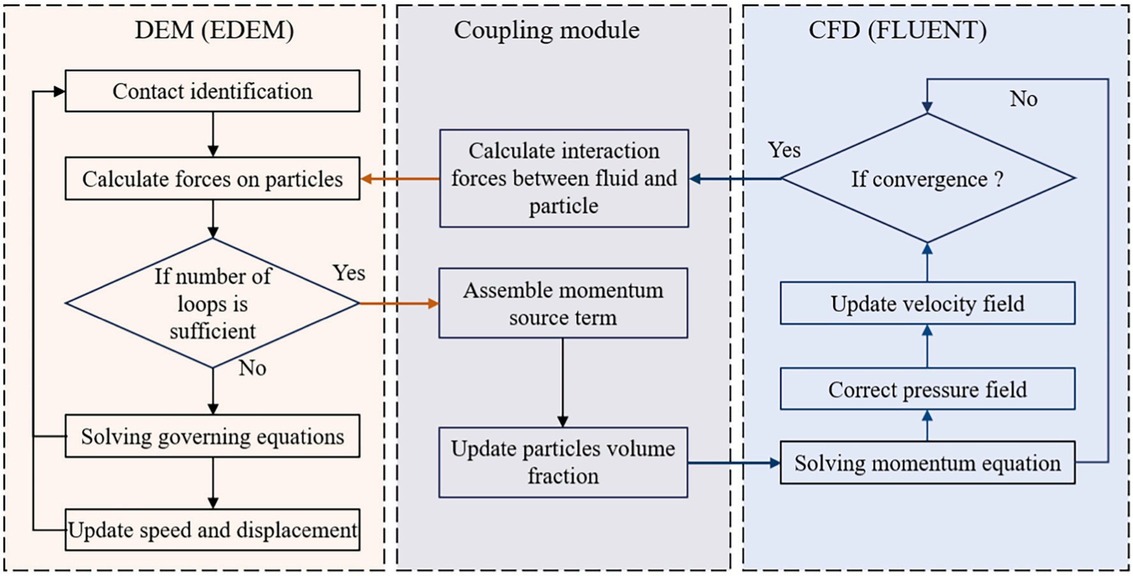

Fig. 3. Diagram of CFD-DEM coupling.

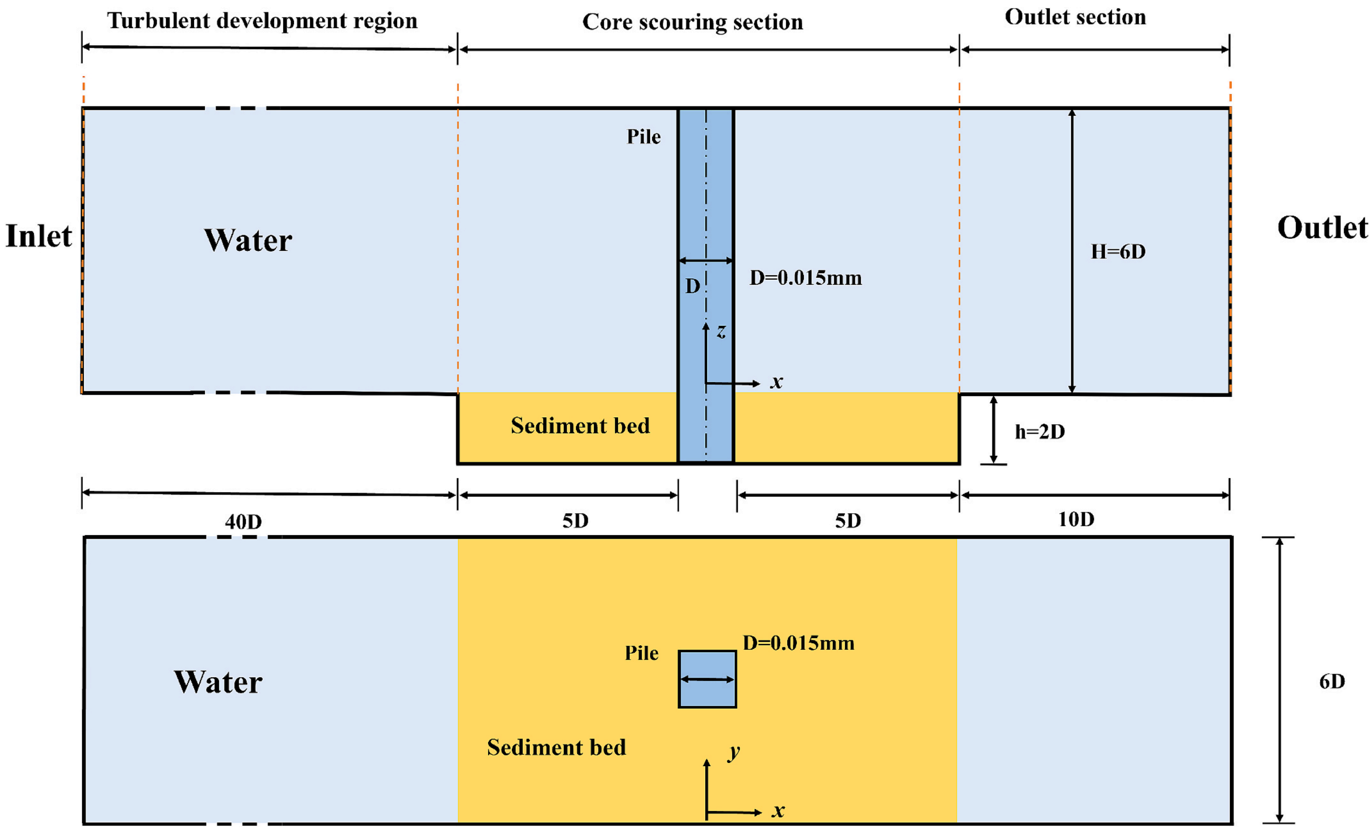

Fig. 4. Schematic diagram of the coupled CFD-DEM model for the local scour around a pile.

the resultant external forces and torques acting on each particle in the next time step, thereby driving the continued motion of the particles. This two-way coupled process iterates cyclically with each time step until the entire simulation duration is completed, ultimately achieving a full-cycle dynamic coupled simulation of the fluid–particle system. The flow chart of the coupling process is illustrated in Fig. 3. Single scour event simulation was run for 20 s of real physical time. This simulation was completed in 15 days on a computing platform equipped with two Intel Xeon Platinum 8488C processors, each containing 48 cores, for a total of 96 cores.

3. Simulation procedures

3.1. Model parameters

The structure of the computational domain and the coupled numerical model is illustrated in Fig. 4. The pile diameter (D) is set as 15 mm. The main computational domain is a rectangular flume with a total

Table 1
Input parameters for CFD and DEM modeling.

Model	Type of parameter (unit)	Parameter value
DEM	Number of particles	1.00×10^5
	Particle size (mm)	1, 2
	Particle density (kg/m^3)	2.65×10^3
	Shear modulus (MPa)	5
	Poisson's ratio, ν	0.35
	Coefficient of friction between particles	0.45
	Coefficient of rolling friction between particles	0.1
	Coefficient of friction between particles and walls	0.5
	Coefficient of rolling friction between particles and walls	0.125
CFD	Fluid density (kg/m^3)	1.00×10^3
	Dynamic viscosity (Pa·s)	1.00×10^{-6}
	Cell Number	38,060
	Velocity (m/s)	0.4 m/s
CFD-DEM	Time step of CFD (s)	1.00×10^{-3}
	Time step of DEM (s)	1.00×10^{-5}
	Coupling Interval (s)	1.00×10^{-3}
	Simulation time (s)	20

length of 61D, including a 40D upstream section and a 10D downstream section relative to the pile. A submerged sediment box is positioned in the mid-rear part of the flume, filled with discrete particles to simulate the sediment bed, with a single pile located at the center of the sediment bed. Along the flow direction, the fluid domain is divided into three main segments: a turbulent development section (40D), a core scouring section (13D), and an outlet section (10D). The turbulent development section is designed to allow full development of the boundary layer, forming a velocity profile consistent with realistic flow conditions. The outlet section, on the other hand, ensures adequate development of the wake vortices behind the pile and minimizes interference from the outflow boundary on the flow structure. To reduce the influence of the free surface and suppress sidewall effects on vortex shedding, the fluid height above the sediment bed is set to 6D, and the width in the y-direction is also set to 6D, thereby effectively mitigating vortex shedding variations induced by boundary effects. In this study, the pile diameter D is used to normalize the dimensions of the computational domain. It should be noted that the simulated region is significantly larger than the pile diameter and that boundary effects are effectively controlled. Furthermore, normalization facilitates direct comparison of the results from this study with other experimental and numerical investigations. The flow in the domain is driven by the water velocity, with the top and side walls treated as impermeable slip walls. The fluid domain is discretized using a uniform grid with a cell size of 0.006 m × 0.006 m × 0.006 m, resulting in a total of 38,060 hexahedral elements.

In the developed CFD–DEM model, the pile is represented as a rigid, impermeable, and stationary boundary. Given its negligible deformation during scouring compared to soil deformation and the characteristic geometric scale, the pile is treated as absolutely rigid. The friction coefficient between the pile wall and particles (see Table 1) is set based on established experimental data for similar interfaces. Within EDEM, the pile acts as a fixed rigid boundary interacting with particles via the Hertz-Mindlin contact model, while in Fluent, its surface is defined as a no-slip wall. The evolution of the bed morphology due to scouring is captured through bidirectional CFD–DEM coupling. Specifically, the real-time particle positions from the EDEM module are used to dynamically reconstruct the fluid–solid interface in the CFD domain, thereby reflecting morphological changes. Throughout the simulation, the geometric boundary of the stationary pile remains fixed. Data exchange between the two domains is facilitated by user-defined functions (UDFs) on the Fluent–EDEM interface platform. The coupling scheme iterates cyclically over each time step until the entire simulation duration is completed, achieving a fully dynamic, coupled simulation of the fluid–particle system.

In the DEM setup, the particle system was modeled as an idealized, well-graded sand comprising perfectly spherical particles. The sand consisted of two discrete particle sizes: $d_1 = 1$ mm and $d_2 = 2$ mm. To improve computational efficiency while preserving accuracy in key regions, the sediment bed DEM model was optimized by adopting a particle size refinement strategy (Zhang et al., 2023). The sediment bed thickness was set to 2D, consistent with the observed morphological features of local scour pits in practical engineering applications. Specifically, a dual-particle-size configuration scheme was implemented, as shown in Fig. 5. In the high-disturbance zone near the pile and the bed surface, uniform particles with a diameter of $d_1 = 1$ mm were used. This zone is defined as the area within a depth of 0.5D below the bed surface and within a horizontal distance of D from the pile center. In contrast, in the deep and far-field regions where significant deformation does not occur during the scour process, particles with diameter d_2=2mm were adopted. This strategy ensures simulation accuracy in critical regions while significantly reducing the computational resource demands of the DEM simulation. The parameter values for the coupled CFD-DEM model are provided in Table 1, with parameter values referenced from previous studies (Zheng et al., 2025; Zhang et al., 2025).

The simulation procedure for local scour around a single pile comprises four consecutive steps: pile configuration, particle generation, sediment deposition and flow initiation. To investigate the influence of pile shape on flow characteristics and scour evolution, five distinct pile geometries were designed, with the geometric parameters of their cross-sections illustrated in Fig. 6. The rounded corner ratio is defined as *R/D*, where *R* represents the corner radius and D denotes the cross-sectional dimension of the pile. In this study, D was set to 15 mm, while *R* was

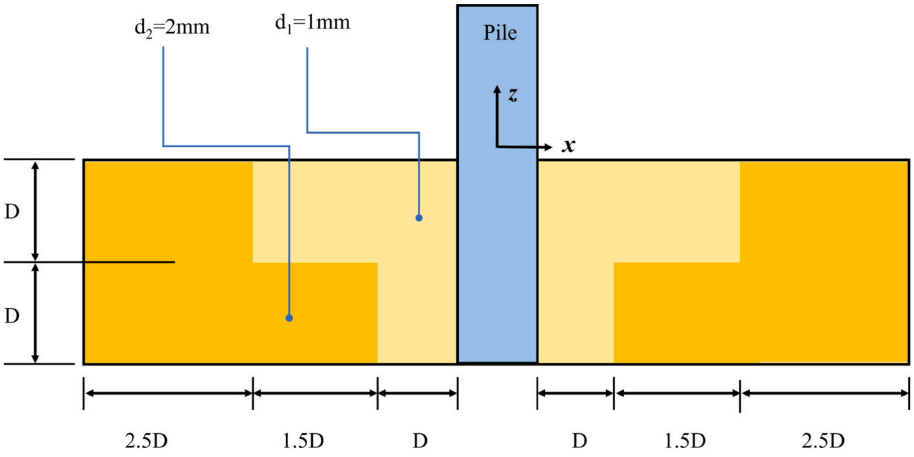

Fig. 5. Spatial distribution of discrete sediment particles in the DEM model.

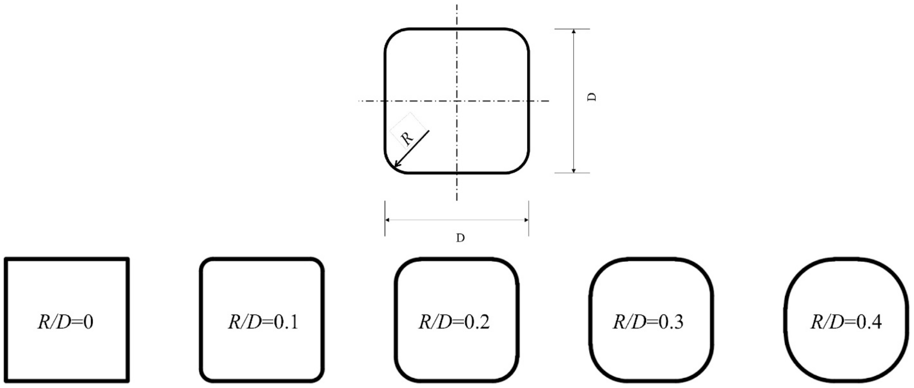

Fig. 6. Schematic of model cross-section parameters.

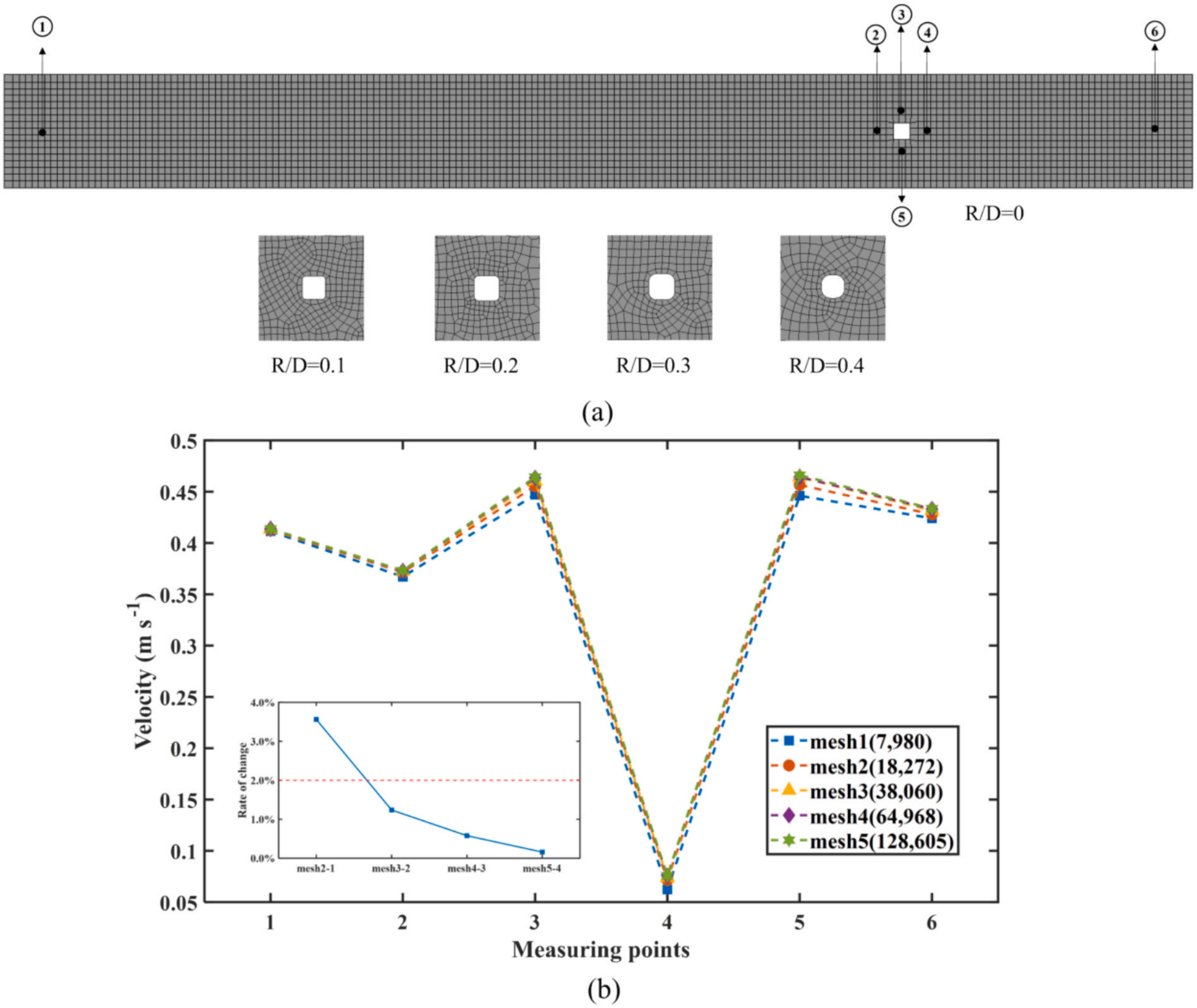

Fig. 7. Mesh independence analysis: (a) Locations of sampling points; (b) Velocity differences for five mesh resolutions.

varied from 0 mm to 6 mm at intervals of 1.5 mm, corresponding to a rounded corner ratio range of 0 to 0.4. It should be noted that, it was found that square piles with rounded corners exhibit a narrower scour extent and a lower maximum scour depth compared to standard circular piles (Li et al., 2025). Therefore, to focus on the evolution of scour behavior influenced by pile geometry, the present analysis was limited to *R/D* ratios ranging from 0 to 0.4.

3.2. *Mesh sensitivity analysis*

To evaluate the influence of grid density on the numerical simulation results, a grid independence study was carried out. Five grid models with cell counts of 7980, 18,272, 38,060, 64,968, and 128,605 were designed. Fig. 7(a) compares the fluid velocity distributions at sampling points for the different grids. It can be observed from Fig. 7(b) that when the number of grid cells increases to 18,272, the deviation of the obtained velocity values from those on coarser grids is now less than 2%,

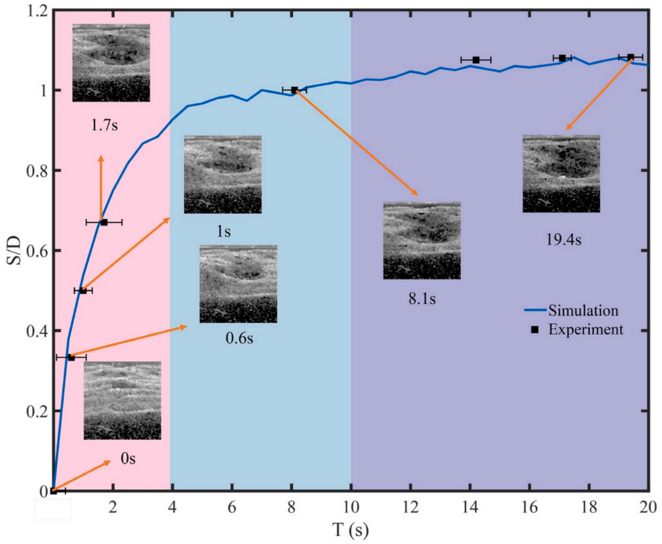

Fig. 8. Development of the maximum scour depth in front of the pile.

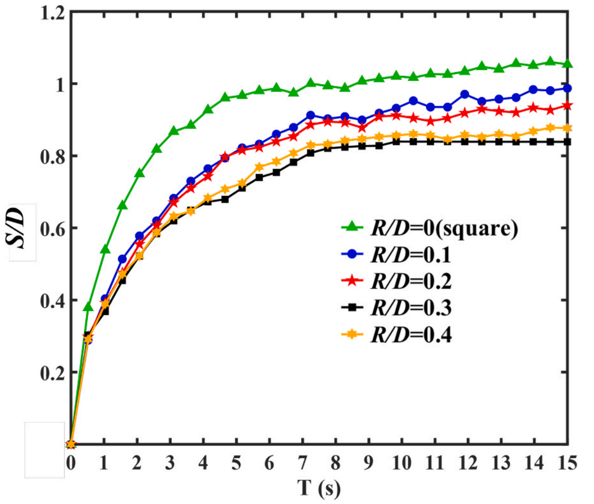

Fig. 9. Evolution of normalized scour depth (S/D) for different rounded corner ratios (R/D).

indicating that further grid refinement has a limited effect on the results, thus verifying grid independence (Ji et al., 2025). To accurately represent the geometric details of the pile configuration while maintaining computational efficiency, the grid with 38,060 cells was selected for subsequent simulations. This choice achieves a good balance between numerical accuracy and computational cost. In addition, the orthogonal quality of this grid is 0.8537, which exceeds the Fluent solver's required threshold of 0.3, thereby satisfying the stability criteria for the numerical computation.

3.3. Verifications

To ensure the reliability of the numerical model, the key parameters in the simulations—such as the pile diameter, sediment size, and flow velocity—were strictly aligned with the experimental setup detailed in Section 2.1. Furthermore, to establish a direct correspondence in the temporal domain, real physical time steps were employed in the coupled CFD-DEM calculations. Consequently, the time variable output from the simulations (e.g., "Time" on the abscissa of Fig. 8) corresponds directly to the physical time recorded in the experiments (in seconds). This alignment establishes a direct, one-to-one correspondence between the simulation results and experimental data for validation. To validate the numerical methodology for simulating solid–fluid interactions around a pile, the simulation results are compared with experimental and numerical data. Fig. 8 illustrates the temporal variation of the relative scour depth S/D (where S is the scour depth around the pile). The developed CFD–DEM model accurately captures the evolution of scour depth and provides a reliable prediction of the equilibrium relative scour depth. The evolution of scour depth is generally divided into three distinct phases. The initial phase exhibits a rapid increase in scour depth ahead of the pile. The deceleration phase involves a progressive decline in scour rate, with the time required to attain a given scour depth increasing significantly. The stable phase sees the maximum scour depth approach an equilibrium condition, and the development of the local scour pit around the pile largely ceases. Photographs of the pile and surrounding particle bed taken during the experiments are also presented in the Fig. 8. The experimental data points represent the time required to reach a specific scour depth, and their horizontal error bars originate from the variability in time across three independent repeated experiments. The comparison reveals that the numerical simulations agree well with the experimental measurements, although minor discrepancies are observed. These deviations may be attributed to the non-spherical shape of real sediment particles, whereas the DEM model simplifies particles as spheres. Other potential influencing factors, such as undetected vibrations, ambient temperature variations, or particle surface contamination, may also have contributed to the differences. Overall, the consistency between the simulation and experimental results is satisfactory. Thus, the CFD–DEM approach employed herein can effectively predict the development of local scour around the pile.

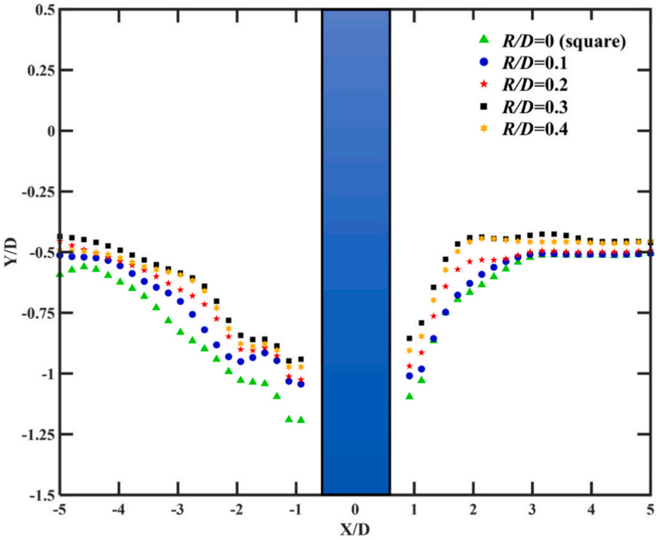

Fig. 10. Scour pit profiles at y = 0 with different R/D.

4. Results and discussion

4.1. Particle bed characteristics

Fig. 9 presents the temporal evolution of the normalized scour depth (S/D) in front of the pile for different rounded corner ratios ($R/D = 0$, 0.1, 0.2, 0.3, 0.4), based on CFD-DEM simulation results. The scour depth is derived from the displacement of surface sediment particles and reflects the influence of pile on local scour development. Across all cases, the scour evolution follows three characteristic stages: a rapid initial growth phase, a deceleration phase and a stabilization phase. Among the simulated operating conditions, the square pile ($R/D = 0$) develops scour most rapidly and reaches the deepest equilibrium depth. In contrast, the rounded-corner piles ($R/D > 0$) exhibit significantly

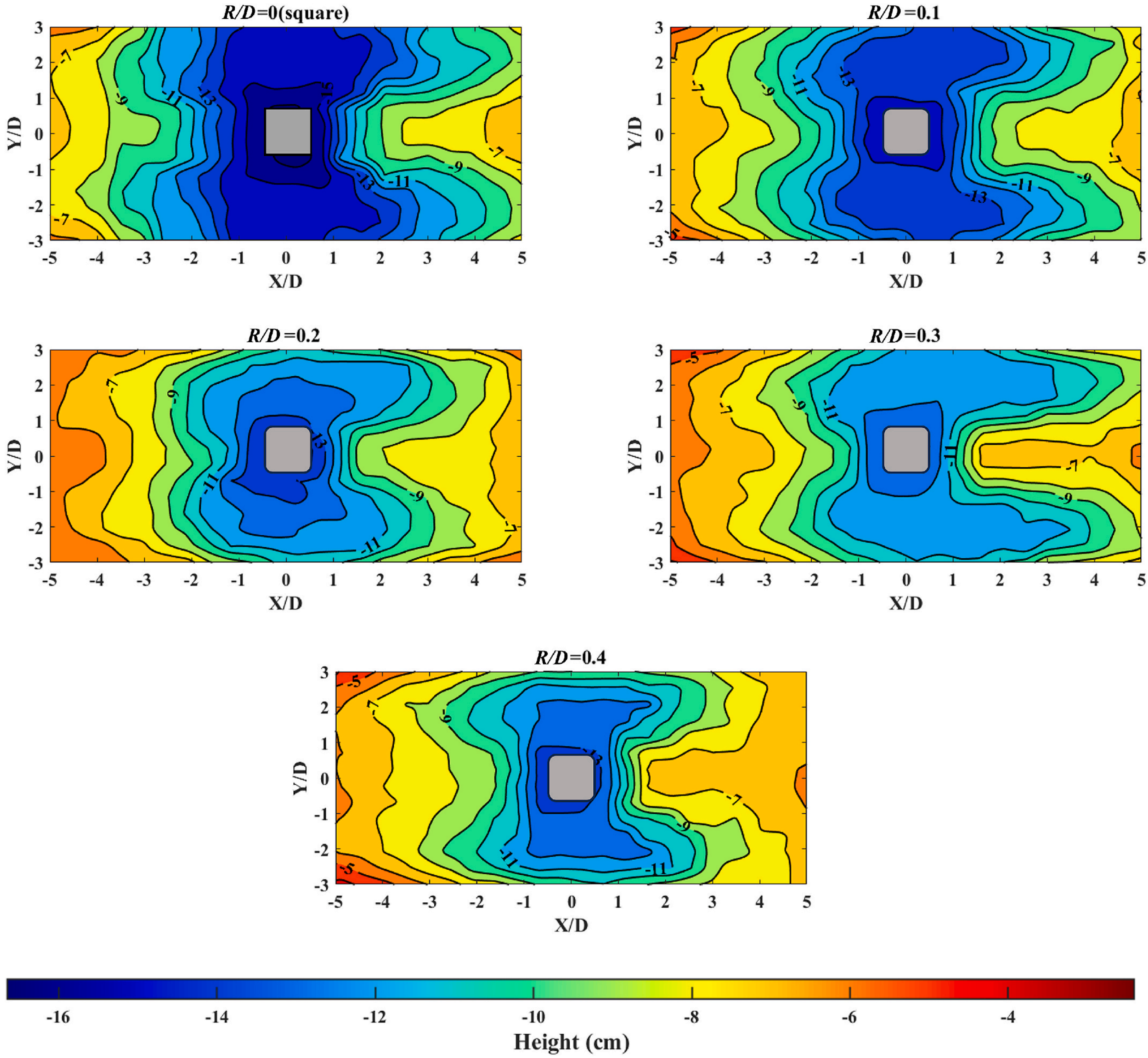

Fig. 11. Bed elevation contours around the pile for different R/D after scour.

smaller scour depths. This can be primarily attributed to the presence of rounded corners, which smoothen the foundational geometry and reduce the flow resistance exerted by the pile on the water flow, thereby decreasing sediment transport and reducing the overall scour depth. Notably, the $R/D = 0.3$ configuration provides the most favorable performance among the rounded cases. Compared with smaller radii ($R/D = 0.1$ and 0.2), $R/D = 0.3$ produces a slower initial scour rate and achieves equilibrium earlier (around 10 s). This suggests that increasing the rounded corner ratios can further reduce the flow resistance around the pile, thereby further mitigating the extent of local scour. Compared with the larger-radius case ($R/D = 0.4$), although the final scour depths are similar, the $R/D = 0.3$ curve is smoother and more stable, with fewer fluctuations and a more compact scour pit. At equilibrium, the S/D value for $R/D = 0$ is one-third higher than that for $R/D = 0.3$. Based on the above, it can be inferred that an R/D ratio of 0.3 may be optimal for mitigating local scour.

To further investigate the development of scour pit morphology, Fig. 10 presents lateral bed profiles at normalized depths under different rounded corner ratios around the pile. These profile results further demonstrate that increasing the corner radius can effectively mitigate local scour around the pile. It is observed that the square pile ($R/D = 0$) produces the deepest scour near the toe, with steep bed slopes on both sides. The slope on the right is greater than that on the left, indicating that the scour development rate at the rear of the pile is slower than at the front. As the corner radius increases, the scour depth in the upstream region gradually decreases, and the bed slope becomes milder. Among all cases examined, $R/D = 0.3$ demonstrates the most favorable performance. Compared to the cases with smaller radii ($R/D = 0.1$ and 0.2), it achieves a moderate scour depth alongside a smoother bed profile. In contrast to the case with the larger radius ($R/D = 0.4$), the scour profile for $R/D = 0.3$ is more compact and stable. This indicates that beyond an optimal point, increased rounding does not improve scour resistance but may promote lateral expansion of the scour pit. These results confirm that introducing a rounded corner can effectively reduce local scour by

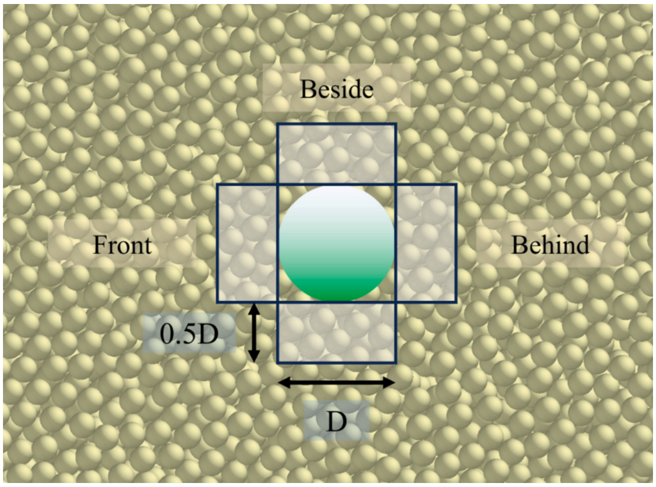

Fig. 12. Zoning of sediment particles around the pile.

decreasing the flow resistance induced by the pile. Notably, $R/D = 0.3$ achieves an optimal balance between scour depth control and bed morphology stability, highlighting its potential for practical application in the design of pile foundations.

The trends observed in these profiles are further illustrated by the contour plot of the stabilized bed morphology. Fig. 11 shows the scour patterns around the pile with different rounded corner ratios from the numerical simulation. It reveals that local scour is mainly concentrated around the pile. There, sediment particles are eroded and transported downstream. They are eventually deposited at the rear of the pile. The scour morphology clearly reflects the significant influence of foundation geometry on both the extent and intensity of local scour, with contour lines indicating local bed elevation and darker blue shades denoting greater scour depths. The square pile ($R/D = 0$) exhibits the most severe scour, characterized by a deep scour pit (>16 cm) concentrated in the front region with steep side slopes and notable lateral expansion. As the corner radius increases, the maximum scour depth gradually decreases, and the scour pit evolves toward a shallower and more symmetrical shape. The optimal anti-scour performance is achieved at $R/D = 0.3$, which corresponds to the minimum scour depth and the most compact and regular scour pit geometry. In contrast, a further increase in R/D to 0.4 leads to a slight enlargement in both scour depth and lateral expansion. These morphological variations suggest that changes in pile geometry effectively alter the local flow characteristics. Overall, the results demonstrate that an appropriate rounding strategy, particularly at $R/D = 0.3$, most effectively mitigates local scour development around the pile.

4.2. *Evolution of kinetics of particles*

To clarify the formation mechanisms of scour pits and investigate the role of localized sediment particle motion during their evolution (Zheng et al., 2025), the kinetic characteristics of sediment particles were analyzed within three representative zones around the pile. These zones include the upstream region (Front), the left and right lateral regions (Besides), and the downstream region (Behind), as illustrated in Fig. 12. Each zone is defined as a rectangular volume with a length equal to the pile diameter D and a width of 0.5D, extending vertically to the seabed depth. The total kinetic energy E_k, which includes both translational kinetic energy E_{kt} and rotational kinetic energy E_{kr}, was calculated to quantify particle activity. The expression is given by:

$$E_k = \sum_{i=1}^{k} \left(\frac{1}{2} m_i {U_i}^2 + \frac{1}{2} I_i {\omega_i}^2 \right) \tag{14}$$

The change in particle bed morphology is directly attributed to variations in particle kinetic energy. Fig. 13 illustrates the distribution of E_{kt} and E_{kr} around the pile under different rounded corner ratios. It should be noted that detached floating particles, which have negligible influence on scour development, were excluded from the kinetic energy calculation. The stacked bars show the kinetic energy contributions in front of, besides, and behind the pile. The black line corresponds to the total kinetic energy. The square pile ($R/D = 0$) exhibits the highest total kinetic energy of particles. This finding aligns with the most severe scour morphology observed in Fig. 8. As the rounded corner radius increases, both translational and rotational kinetic energies gradually decrease, with the most significant reduction occurring at $R/D = 0.3$. Across all

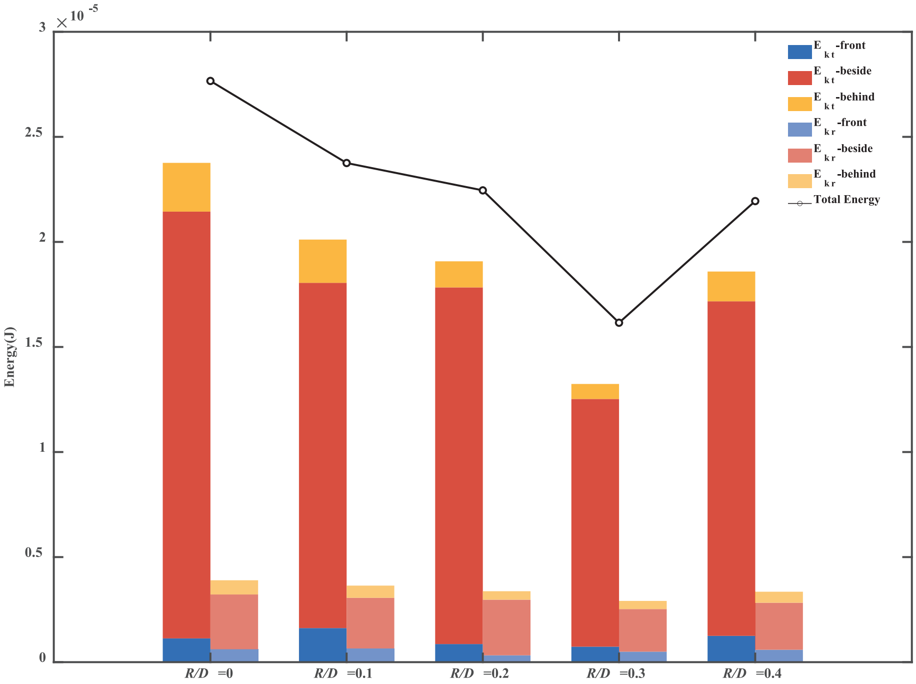

Fig. 13. Total kinetic energy and its translational and rotational components around the pile with different R/D.

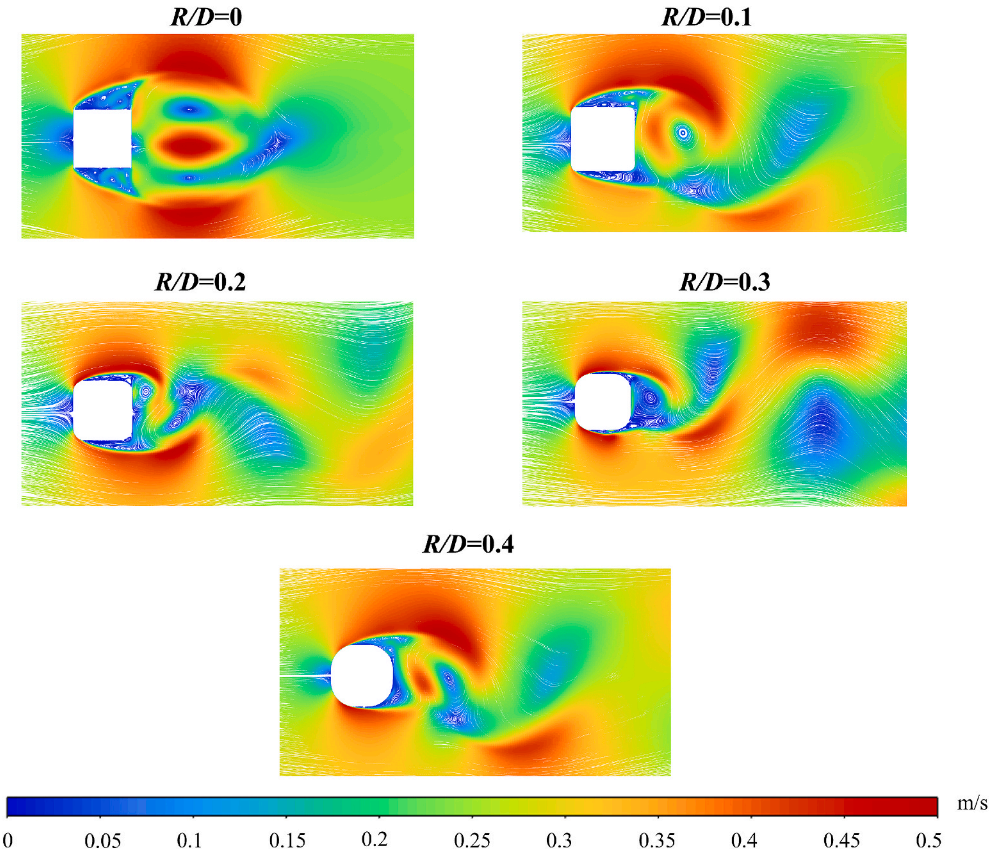

Fig. 14. Instantaneous streamlines and velocity contours on the x-y plane for piles with different *R*/*D*.

cases, translational kinetic energy consistently exceeds rotational kinetic energy, accounting for approximately 70%–85% of the total, indicating that sediment transport during the scouring process is predominantly translational. It can be reasonably inferred that a large number of particles are lifted from the seabed, behaving as suspended sediment with motion characterized mainly by translation. Higher translational kinetic energy reflects stronger particle mobility, thereby leading to more intense scouring. Furthermore, the lateral kinetic energy contribution is consistently greater than that in front of and behind the pile, correlating with the deeper scour pits observed beside the pile in the bed morphology results. It is noteworthy that the $R/D = 0.3$ case exhibits the lowest total kinetic energy, suggesting that this configuration most effectively suppresses turbulence generation and sediment entrainment. In contrast, a slight rebound in kinetic energy is observed at $R/D = 0.4$, indicating that excessive rounding may redistribute rather than further reduce energy. These results demonstrate a close relationship between local energy distribution and scour evolution, highlighting the effectiveness of moderate rounding (particularly $R/D = 0.3$) in mitigating scouring by controlling turbulence.

4.3. Evolutions of flow characteristics

In order to investigate the variation in particle kinetic energy, key flow field characteristics were extracted. The analysis plane was placed at the mid-depth position (z/H = 0.5, where H is the water depth). This choice aims to minimize the influence of the bed boundary layer, thereby ensuring that the observed differences in flow patterns are primarily attributable to changes in geometry. To this end, the subsequent scouring processes are primarily governed by these underlying flow structures. Fig. 14 illustrates the instantaneous streamline patterns and velocity contours in the x-y plane around a pile with different rounded corner ratios. The results demonstrate the significant regulatory effect of the corner radius on the flow separation structure and wake evolution. As R/D increases, systematic changes occur in the separation position, shear layer development, and vortex structure in the wake, indicating a transition of the flow field from an unstable to a more stable state. For the square pile ($R/D = 0$), the incoming flow separates markedly at the upstream leading edge, forming a typical dual shear layer structure. A large-scale recirculation zone appears behind the pile, accompanied by a substantially widened wake with low-velocity characteristics and high velocity gradients within the shear layers. The vortex structures exhibit strong instability, reflecting a highly unsteady flow state. At $R/D = 0.1$ and 0.2, the corner effect begins to emerge: the separation point on the windward edge shifts slightly downstream, and the original large-scale recirculation in the wake weakens or breaks into smaller vortices. The high-velocity region moves closer to the pile surface, and the streamlines become smoother, indicating enhanced flow attachment and reduced energy transfer within the shear layers. When R/D reaches 0.3, the corner effect becomes optimal. Separation on the windward side is significantly delayed, and high-speed flow remains attached closely to the surface along the rounded corner, promoting more continuous attached flow along the pile. The shear layers develop along both sides and close in the wake, forming only a relatively stable separation vortex. The low-velocity region shrinks considerably, and the wake narrows with improved symmetry, demonstrating enhanced flow stability and reduced energy dissipation. This flow configuration effectively reduces total drag by delaying separation and promoting shear-layer attachment, while also suppressing unsteady vortex shedding, representing an optimal balance in aerodynamic performance. With a further increase to $R/D = 0.4$, the attached flow on the windward side weakens slightly, and the flow path deviates somewhat from the surface. Moreover, an excessively large corner radius adversely affects wake symmetry, causing a shift in the separation vortex position and a slight decline in overall flow stability. The smoothing of the base geometry by rounding

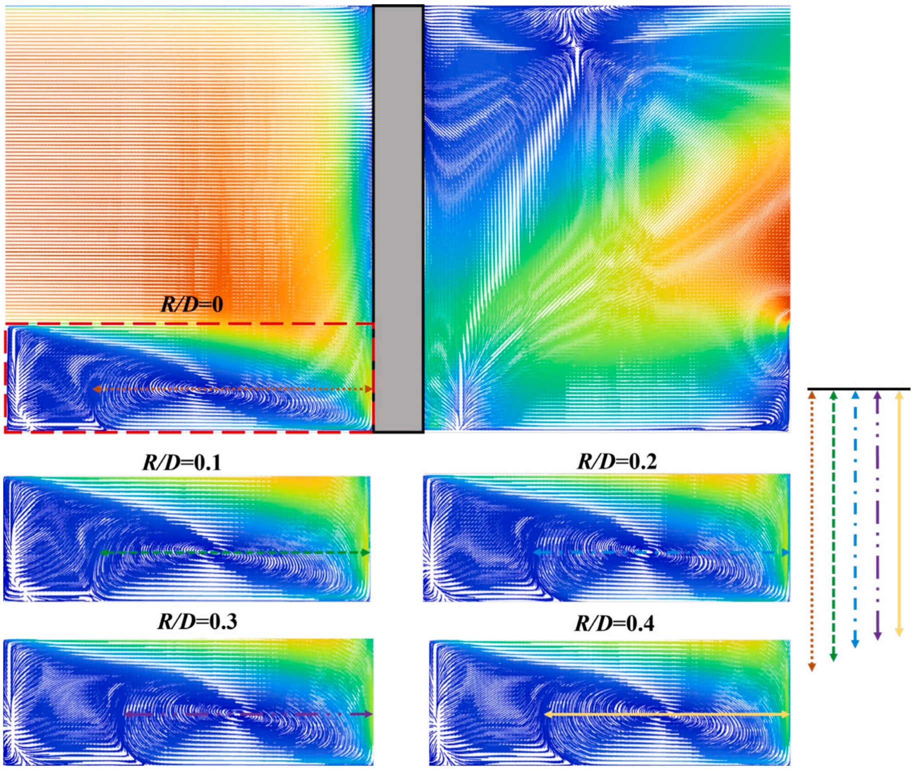

Fig. 15. Instantaneous streamlines and velocity contours on the x-z plane for piles with different *R/D*.

generally delays separation, weakens vortex intensity, and consequently helps reduce local sediment transport capacity and overall scour depth around the pile.

The evolution of these large-scale flow structures directly influences near-bed flow characteristics, particularly the morphology of the horseshoe vortex associated with scour development. Fig. 15 presents instantaneous streamlines and velocity distributions on the pile's x–z cross-section for different rounded corner ratios (R/D). The red-dashed area marks the key near-bed control zone, where downwash–horseshoe vortex interaction governs sediment initiation and scour. Specifically, incoming flow impinges on the pile's leading face, forming a downwash jet that creates a near-bed high-velocity region. Subsequent flow separation induces counter-rotating horseshoe vortices, forming a high-shear recirculation zone. As the corner ratio (R/D) increases from 0 to 0.4, the near-bed flow exhibits a systematic variation. Colored arrows in the figure are used to provide an intuitive overview of the evolution in scale and intensity of the key flow structure—the horseshoe vortex—under different R/D conditions. Specifically: at $R/D = 0$ (corresponding to the red arrow), the strong downwash flow induces a large-scale, high-intensity horseshoe vortex, resulting in concentrated streamlines, intense vortical motion, and increased velocity gradients. Accompanied by strong turbulence and high bed shear stress, this leads to the deepest scour hole. When R/D increases to 0.1 and 0.2 (corresponding to the green and blue arrows, respectively), the rounding effect becomes apparent: the downwash flow weakens, the scale of the horseshoe vortex decreases significantly, and the streamlines become smoother. This reduces local entrainment, lowers the velocity gradient and turbulent kinetic energy near the pile toe, expands the low-velocity zone, contracts the separation zone, alleviates the concentration of shear stress, and thereby significantly reduces the scour depth. Under $R/D = 0.3$ (corresponding to the purple arrow), the flow is most stable. The horseshoe vortex reaches a steady and weakened state with a uniform velocity distribution. Weakened entrainment and recirculation suppress turbulence, minimize bed shear stress, produce the shallowest scour hole, achieve maximum suppression of flow separation, and optimize the distribution of flow energy. When R/D further increases to 0.4 (corresponding to the yellow arrow), the front high-velocity zone expands slightly, but the vortex scale remains similar to that at $R/D = 0.3$, indicating that a further increase in the corner radius does not provide additional vortex suppression. In summary, horseshoe vortex scale variation with R/D dominates local scour degree. Large vortices with high velocity gradients and strong turbulence exacerbate scouring, while smaller, stable vortices reduce near-bed shear stress and control scour intensity. The $R/D = 0.3$ configuration best balances vortex suppression and flow stability, representing the most effective geometry for scour control.

4.4. *Prediction formula and validation for scour depth*

4.4.1. *Calibration of the prediction formula*

To provide engineering guidance for the prediction of local scour pits and the design of scour protection measures, a quantitative relationship between the maximum local scour depth and the rounded corner ratio of the pile was established based on a modified empirical scour formula. Empirical formulas have been widely adopted to predict the maximum local scour depth around bridge pier foundations. However, they are generally developed for piles with standard cross-sections. To improve the applicability, a shape-related geometric correction factor was introduced. The basic form of the empirical formula is expressed as follows [Ministry of Transport of the People's Republic of China, 2015]:

$$S/D = 1.17k_\varepsilon k_\alpha h_p \left(\frac{l}{h_p}\right)^{0.6} \left(\frac{\overline{d}}{h_p}\right)^{-0.15} \left[\frac{(v - v_0')^2}{g h_p}\right]^{0.15} \tag{15}$$

where k_α is the flow structure angle coefficient, k_ε is the shape coefficient, g is the gravitational acceleration, l is the length of the pile perpendicular to the flow direction, h_p is the local flow depth around the pile after general scour, $\overline{d}$ is the average grain size of the channel sediment, v is the approach velocity after general scour, and v_0' is the critical velocity for incipient sediment motion. This formula comprehensively

Table 2
Parameters used in the scour prediction model.

k_ε	$g(m/s^2)$	$l(m)$	$h_p(m)$	$\bar{d}(m)$
0.39	9.8	0.015	0.08	0.0015

Table 3
Simulated and calculated scour depth for different rounded corner ratios.

R/D	S/D(Simulation)	S/D(calculation)
0	1.055	1.067
0.1	0.991	1.019
0.2	0.945	0.919
0.3	0.845	0.834
0.4	0.882	0.901

Table 4
Validation of the modified scour prediction formula.

R/D	S/D(Simulation)	S/D(calculation)
0.15	0.962	0.977
0.25	0.874	0.862

accounts for the dominant hydrodynamic and sediment-related parameters influencing local scour, including flow velocity, pile orientation relative to the flow direction, and sediment characteristics. The values of the parameters adopted in the present study are summarized in Table 2.

Based on the CFD–DEM simulation results presented in Table 3, a correction function describing the influence of the rounded corner ratio R/D on local scour depth was established. By introducing this function as a geometric modification coefficient into the original empirical formula, the predictive formula was extended to account for rounded-corner square piles. This approach enables quantitative prediction of local scour depth for piles with different corner rounding configurations.

The fitted geometric correction function for the rounded corner ratio is expressed as:

$$f(R/D) = 0.8exp\left(\frac{0.274 \times (R/D - 0.3)^2}{0.02315 + (R/D - 0.28)^2}\right) + 0.0045 \tag{16}$$

By incorporating the rounded corner correction function $f(R/D)$ into Eq. (15), the modified scour depth prediction formula applicable to rounded-corner square piles is obtained as:

$$S/D = 1.17k_\varepsilon f(R/D)k_\alpha h_p\left(\frac{l}{h_p}\right)^{0.6}\left(\frac{\bar{d}}{h_p}\right)^{-0.15}\left[\frac{(v - v_0')^2}{gh_p}\right]^{0.15} \tag{17}$$

4.4.2. Verification of the prediction formula

To evaluate the predictive accuracy of the modified scour depth formula, calculated results were compared with independent CFD–DEM simulation data. The validation cases are summarized in Table 4.

To further assess the robustness and general applicability of the modified prediction formula, additional simulations at intermediate rounded corner were conducted. The predicted maximum local scour depths obtained from Eq. (17) were compared with the corresponding simulation results, as illustrated in Fig. 16. The normalized maximum local scour depth (S/D) exhibits a clear dependence on the rounded corner ratio. The fitted prediction curve derived from the modified formula agrees well with the simulation data over the entire range of R/D considered, with most data points falling within the ±5% error band. This result indicates that the modified formula captures the influence of rounded corner geometry on scour depth with satisfactory accuracy and can provide reliable predictions for rounded-corner square piles under

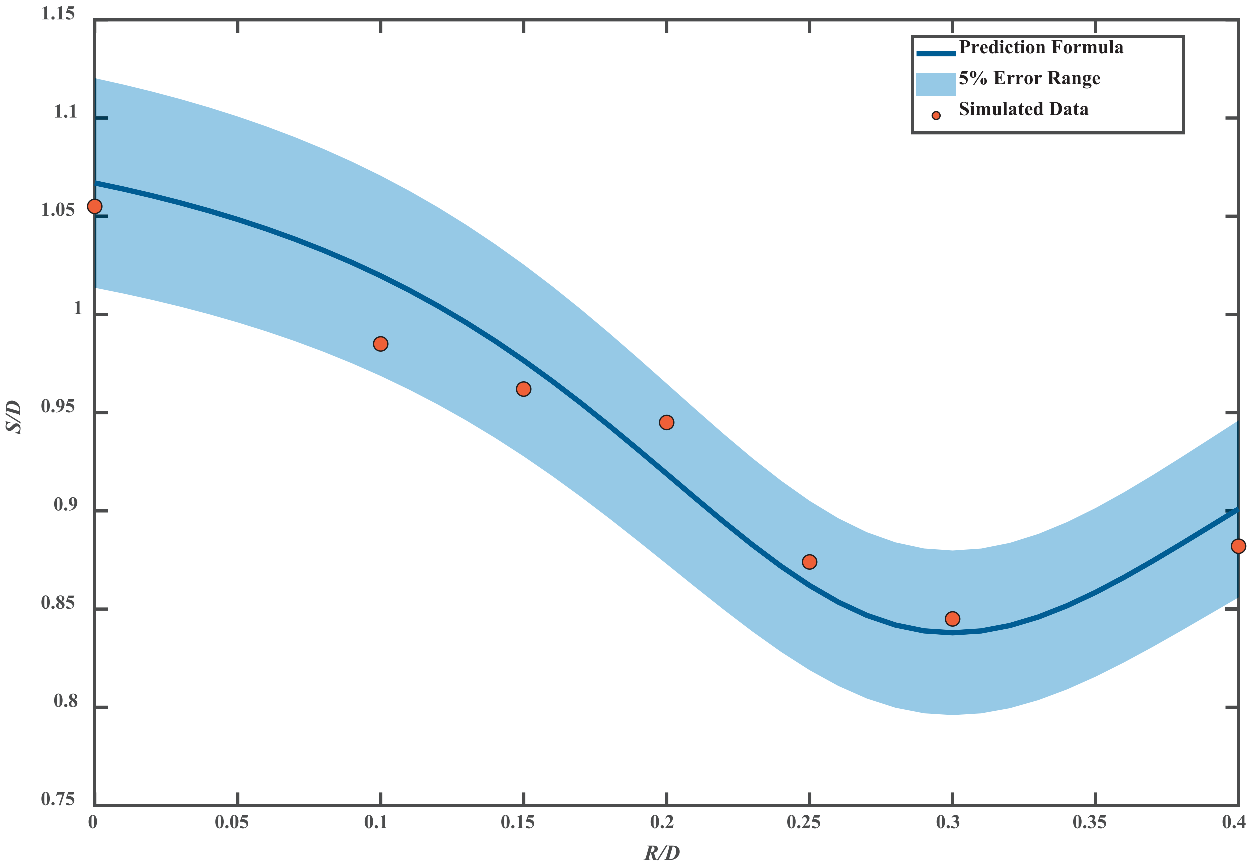

Fig. 16. Comparison between predicted and simulated local scour depth (S/D) as a function of rounded corner ratio (R/D), with ± 5% error band.

clear-water scour conditions.

5. Conclusion

This study investigates local scour around rounded square piles using a coupled CFD–DEM numerical model and confirms its applicability to piles with complex cross-sections. Based on analyses of sediment particle dynamics and near-bed flow structures, the influence of corner rounding on scour development is clarified, and a predictive formula for local scour depth is established.

The local scour process evolves through three characteristic stages, namely rapid scour, deceleration, and equilibrium. The square pile ($R/D = 0$) produces the deepest and steepest scour hole near the pile toe. With increasing rounded corner ratio, the maximum scour depth decreases and the bed profile becomes milder, while the scour morphology transitions from a deep–narrow to a shallow–wide shape. Among the investigated configurations, $R/D = 0.3$ yields the most regular and stable scour profile, indicating an optimal rounded-corner geometry for scour mitigation.

Scour mitigation induced by corner rounding is governed by coupled regulation of sediment particle motion and near-bed flow structures. The square pile exhibits the highest sediment particle kinetic energy and the most severe scour, whereas particle motion is most effectively suppressed at $R/D = 0.3$, where translational kinetic energy dominates sediment transport. From a hydrodynamic perspective, corner rounding weakens downwash intensity and suppresses the development of large-scale horseshoe vortices, thereby stabilizing the flow field and reducing sediment entrainment.

A geometric correction function based on the rounded corner ratio R/D is incorporated into an empirical scour prediction model, resulting in a modified predictive formula applicable to rounded square piles. Validation against CFD–DEM simulation data shows that the prediction error remains within ±5%, demonstrating satisfactory engineering accuracy. The proposed model enables quantitative prediction of local scour depth for non-standard pile geometries and provides a reliable tool for scour risk assessment and anti-scour design optimization of offshore wind turbine foundations.

CRediT authorship contribution statement

Xiangyi Meng: Writing – original draft, Supervision, Funding acquisition. **Yifan Lu:** Writing – review & editing, Methodology, Formal analysis. **Xiaoming Feng:** Investigation, Data curation. **Guizhong Tian:** Supervision, Conceptualization. **Yadong Zhu:** Writing – review & editing, Data curation. **Zhongqiu Mu:** Supervision, Methodology.

Declaration of competing interest

The authors declare that they have no known competing financial interests or personal relationships that could have appeared to influence the work reported in this paper.

Acknowledgements

The authors express their acknowledgment to the Postgraduate Research & Practice Innovation Program of Jiangsu Province (SJCX25_2525) and the Science Research Project of Jiangsu University of Science and Technology (No. 1022932215) for financial support and all of the persons who assisted in this writing.

Data availability

The data that has been used is confidential.

References

Amini Baghbadorani, D., Ataie-Ashtiani, B., Beheshti, A., Hadjzaman, M., Jamali, M., 2018. Prediction of current-induced local scour around complex piers: review, revisit, and integration. Coast. Eng. 133, 43–58. https://doi.org/10.1016/j.coastaleng.2017.12.006.

Baykal, C., Sumer, B.M., Fuhrman, D.R., Jacobsen, N.G., Fredsøe, J., 2017. Numerical simulation of scour and backfilling processes around a circular pile in waves. Coast. Eng. 122, 87–107. https://doi.org/10.1016/j.coastaleng.2017.01.004.

Bordbar, A., Sharifi, S., Hemida, H., 2021. Investigation of the flow behaviour and local scour around single square-shaped cylinders at different positions in live-bed. Ocean Eng. 238, 109772. https://doi.org/10.1016/j.oceaneng.2021.109772.

Chen, J., 2026. Research status and prospects of in-situ installation technology for floating offshore wind turbine. Ocean Eng. 343, 123253. https://doi.org/10.1016/j.oceaneng.2025.123253.

Du, S., Wu, G., Zhu, D.Z., Wang, R., Lu, Y., Liang, B., 2022. Experimental study of local scour around submerged square piles in combined waves and current. Ocean Eng. 266, 113176. https://doi.org/10.1016/j.oceaneng.2022.113176.

Hu, Z., Zhang, Y., Yang, Z., 2019. Suffusion-induced deformation and microstructural change of granular soils: a coupled CFD–DEM study. Acta Geotech. 14, 795–814. https://doi.org/10.1007/s11440-019-00789-8.

Jalal, H.K., Hassan, W.H., 2020. Effect of bridge pier shape on depth of scour. Adv. Mater. Sci. Eng. 671, 012001. https://doi.org/10.1088/1757-899X/671/1/012001.

Ji, S., Li, A., Han, Y., Li, H., Sun, Z., Zhao, D., Gao, H., 2025. Numerical study on the influence mechanism of feed rate on separation quality in a multi-baffle separation duct. Biosyst. Eng. 258, 104258. https://doi.org/10.1016/j.biosystemseng.2025.104258.

Li, D., Zheng, Z., Hu, Z., Ma, H., 2025. Microscopic investigation of shape effect on local scour around the monopile using CFD-DEM. Comput. Geotech. 177, 106872. https://doi.org/10.1016/j.compgeo.2024.106872.

Li, J., Fuhrman, D.R., Kong, X., Xie, M., Yang, Y., 2021. Three-dimensional numerical simulation of wave-induced scour around a pile on a sloping beach. Ocean Eng. 233, 109174. https://doi.org/10.1016/j.oceaneng.2021.109174.

Li, J., Tao, J., 2018. CFD-DEM two-way coupled numerical simulation of bridge local scour behavior under clear-water conditions. Transport. Res. Record: J. Transport. Res. Board 2672, 107–117. https://doi.org/10.1177/0361198118783170.

Li, P., Jiang, J., Li, Q., Ren, Z., 2023. Axial compression performance and optimum design of round-cornered square CFST with high-strength materials. J. Build. Eng. 68, 106145. https://doi.org/10.1016/j.jobe.2023.106145.

Li, Q., Wang, X., Gavin, K., Jiang, S., Diao, H., Wang, M., Wang, K., 2024. Scour effect on the lateral bearing behaviour of monopiles considering different slenderness ratios. Water 16, 226. https://doi.org/10.3390/w16020226.

Liu, L., Wu, M., Chen, G., Tang, Y., Song, X., Zou, M., Xu, Y., Zhang, X., Wang, S., Lv, J., Zheng, L., 2026. Satellite observations and deep learning unveil the rapid expansion of offshore wind turbines in China. Resour. Conserv. Recycl. 227, 108706. https://doi.org/10.1016/j.resconrec.2025.108706.

Liu, X., García, M.H., 2008. Three-dimensional numerical model with free water surface and mesh deformation for local sediment scour. J. Waterw. Port Coast. Ocean Eng. 134, 203–217. https://doi.org/10.1061/(ASCE)0733-950X(2008)134:4(203).

Ma, H., Zhang, S., Li, B., 2023. Numerical investigation of local scour around twin piles under steady current using CFD-DEM coupling method. Comput. Geotech. 164, 105805. https://doi.org/10.1016/j.compgeo.2023.105805.

Ma, H., Zhang, S., Li, B., Huang, W., 2024. Local scour around the monopile based on the CFD-DEM method: experimental and numerical study. Comput. Geotech. 168, 106117. https://doi.org/10.1016/j.compgeo.2024.106117.

Menéndez-Vicente, C., López-Querol, S., Bhattacharya, S., Simons, R., 2023. Numerical study on the effects of scour on monopile foundations for offshore wind turbines: the case of robin Rigg wind farm. Soil Dyn. Earthq. Eng. 167, 107803. https://doi.org/10.1016/j.soildyn.2023.107803.

Meng, X., Zhu, Y., Mu, Z., Tian, G., Feng, X., Zhang, B., Pei, Y., Lu, Y., 2025. DEM-DDM study on the humidification uniformity of brown rice in a pan coater. Biosyst. Eng. 254, 104158. https://doi.org/10.1016/j.biosystemseng.2025.104158.

Mir, B.H., Lone, M.A., Bhat, J.A., 2019. Laboratory investigation for development of local scour depth model for varying shapes of obstruction. Int. J. Hydrol. Sci. Technol. 9, 303311. https://doi.org/10.1504/ijhst.2019.102319.

Mindlin, R.D., Deresiewicz, H., 1953. Elastic spheres in contact under varying oblique forces. J. Appl. Mech. 20 (3), 327–344. https://doi.org/10.1115/1.4010702.

Ministry of Transport of the People's Republic of China, 2015. Hydrological Specifications for Survey and Design of Highway Engineering (JTG C30–2015). China Communications Press, Beijing, China, pp. 29–36. https://xxgk.mot.gov.cn/2020/jigou/glj/202006/P020240607596475014848.pdf.

Olsen, N.R.B., Melaaen, M.C., 1993. Three-dimensional calculation of scour around cylinders. J. Hydraul. Eng. 119, 1048–1054. https://doi.org/10.1061/(ASCE)0733-9429(1993)119:9(1048).

Prendergast, L.J., Gavin, K., Doherty, P., 2015. An investigation into the effect of scour on the natural frequency of an offshore wind turbine. Ocean Eng. 101, 1–11. https://doi.org/10.1016/j.oceaneng.2015.04.017.

Roulund, A., Sumer, B.M., Fredsøe, J., Michelsen, J., 2005. Numerical and experimental investigation of flow and scour around a circular pile. J. Fluid Mech. 534, 351–401. https://doi.org/10.1017/S0022112005004507.

Song, S., Park, S., 2022. Unresolved CFD and DEM coupled simulations on scour around a subsea pipeline. J. Marine Sci. Eng. 10, 556. https://doi.org/10.3390/jmse10050556.

Wang, G., Xu, S., Zhang, Q., Zhang, J., 2023. An experimental study of the local scour protection methods around the monopile foundation of offshore wind turbines. Ocean Eng. 273, 113957. https://doi.org/10.1016/j.oceaneng.2023.113957.

Yang, Q., Yu, C., Liu, X., Yu, W., Jiang, H., 2024. Study on the aerodynamic characteristics and flow mechanism of square cylinders with rounded corners. Structures 62, 106298. https://doi.org/10.1016/j.istruc.2024.106298.

Yazdanfar, Z., Lester, D., Robert, D., Setunge, S., 2021. A novel CFD-DEM upscaling method for prediction of scour under live-bed conditions. Ocean Eng. 220, 108442. https://doi.org/10.1016/j.oceaneng.2020.108442.

Zhang, N., Qiu, G., Zhao, W., Zhai, W., Yin, S., Zheng, Y., 2026. Scour around offshore wind turbine monopile foundations under tidal flow: CFD-DEM coupled approach. Ocean Eng. 343, 123411. https://doi.org/10.1016/j.oceaneng.2025.123411.

Zhang, P., Mu, L., Huang, M., Gu, X., 2025a. Microscopic insights into local scour around a vertical circular pile under steady current: coupled LES-CGDEM simulations. Comput. Geotech. 184, 107248. https://doi.org/10.1016/j.compgeo.2025.107248.

Zhang, S., Li, B., Ma, H., 2023. Numerical investigation of scour around the monopile using CFD-DEM coupling method. Coast. Eng. 183, 104334. https://doi.org/10.1016/j.coastaleng.2023.104334.

Zhang, Y., Zhao, M., Yu, P., Yin, H., Yang, Q., 2025b. Investigation of the bearing capacity and failure envelope of novel umbrella suction anchor foundations in silty soil based on local scour conditions. Comput. Geotech. 188, 107566. https://doi.org/10.1016/j.compgeo.2025.107566.

Zheng, Z., Hu, Z., Ma, H., Huang, W., 2025. Role of sacrificial pile in scour mitigation around the monopile: a multiscale perspective using CFD-DEM. Ocean Eng. 327, 120979. https://doi.org/10.1016/j.oceaneng.2025.120979.

Zheng, Z., Hu, Z., Xie, X., Huang, W., 2024. Local scour around the monopile: a microscopic perspective using CFD-DEM. Ocean Eng. 299, 117318. https://doi.org/10.1016/j.oceaneng.2024.117318.

Zhou, Y.C., Wright, B.D., Yang, R.Y., Xu, B.H., Yu, A.B., 1999. Rolling friction in the dynamic simulation of sandpile formation. Physica A 269, 536–553. https://doi.org/10.1016/S0378-4371(99)00183-1.

Zhu, C., Liu, X., Yang, Q., Zang, W., Liu, H., Liu, X., 2025. Advanced three-dimensional numerical simulation on influence of MS2AF on scour protection considering seabed response: a coupled CFD-FEM method. Ocean Eng. 324, 120625. https://doi.org/10.1016/j.oceaneng.2025.120625.